ELEN90064
Advanced Control Systems

Phase 1 - Single-Link Flexible-Joint Robot

Xing Yang Goh
1001969
Aug 23, 2022

1 Sensor Selection

For the choice of sensor for the system, we will choose between two sensors that directly measure the link angle θ_l instead of the motor angle θ_m. This is because the system is nonlinear such that the relationship between the two angles cannot be consistently determined from the other. Based on this, we will choose between using a vision sensor and a gyroscope. To determine the best sensor for the system, we will create a periodic pulse response from 30° to 60° and analyse how the sensor tracks this reference signal.

1.1 Gyro Sensor

Using the Invensense(ICM-20948) gyro sensor that has the lower drift of $5\frac{deg}{s}$, the following measurements are acquired.

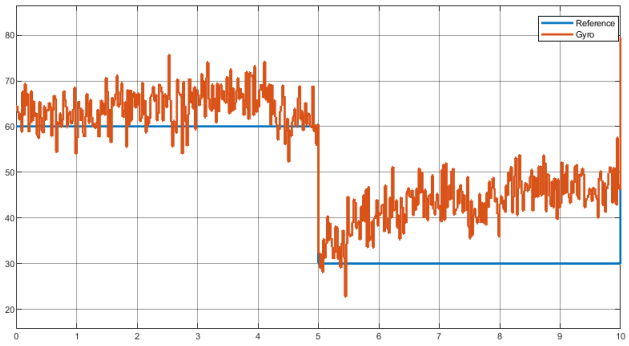

Figure 1: Tracking of the Invesense gyro sensor

The gyro sensor demonstrates a large amount of error, which increases with time due to the phenomenon known as drifting. This occurs since the gyro sensor measures angular accelerations, which requires a double integration to approximate the angular position of the system. Since the sensor is susceptible to measurement noise, this leads to an angular position approximation that deteriorates over time.

1.2 Vision Sensor

The three options for the vision sensor is a capturing at a frame rate of 25, 50 or 100fps and utilises a zero order hold discretisation to provide an angle estimate.

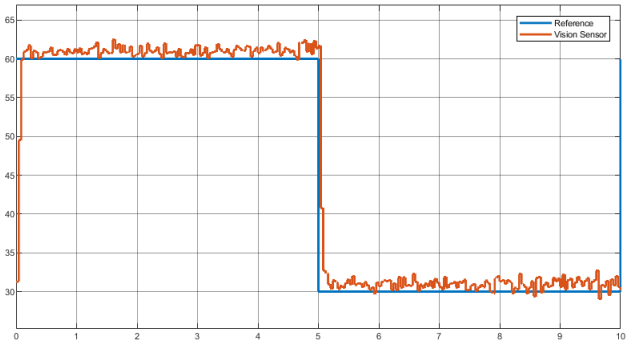

Figure 2: Vision sensor at 25fps

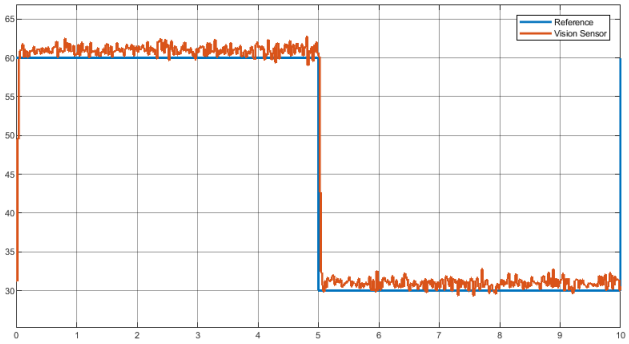

Figure 3: Vision sensor at 50fps

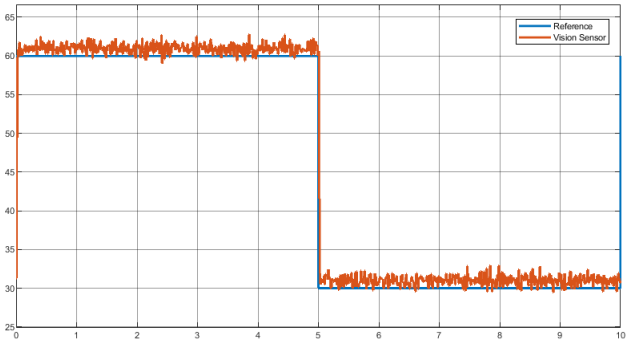

Figure 4: Vision sensor at 100fps

Comparing the performance of the different frame rates, the higher frame rate sensor exhibits a smaller lag between the reference signal and measured signal, apparent when the reference signal changes from 60° to 30°. Furthermore, all 3 sensors exhibits a constant bias term of approximately 1°, which will be calibrated for when in use. Furthermore, all 3 vision sensors exhibits a higher frequency measurement noise. A lowpass filter will be implemented to reduce this variance, however, it is important to account for the phase lag that a LPF will induce, along with a larger overshoot to the tracking. Since the controller will be running at a clock frequency of 50Hz, we use use the vision sensor at 50fps for the performance benefits over the 25fps camera. Using the 100fps camera will reduce the lag of the measurements, however, this will cost 3 times more than the 50fps camera which is not cost-efficient.

2 Plant Analysis

The system a controller will be designed for is a single-link flexible-joint robot as shown in figure 5. The governing equations can be derived using Newton's second law for rotation using the schematic.

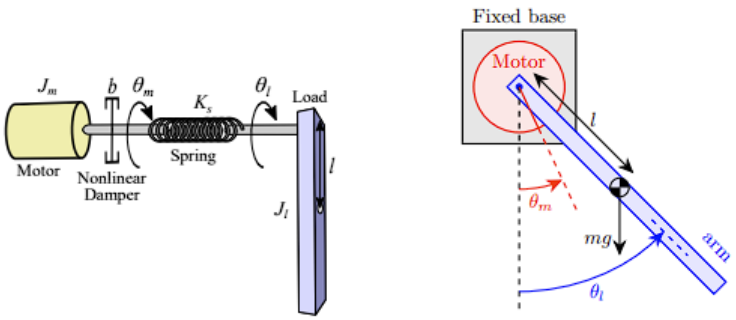

Figure 5: Schematic of a single-link flexible-joint robot

$$J_m\ddot{\theta_m} = K_s(\theta_l - \theta_m) - sgn(\omega_m)b\omega_m^2 + T_m$$

$$J_l\ddot{\theta_l} = -K_s(\theta_l - \theta_m) + mgl\sin\theta_l$$

Rearranging these equations, we have the following EOMs that describe the dynamics of the plant.

$$\ddot{\theta_m} = \frac{K_s}{J_m}\theta_l - \frac{K_s}{J_m}\theta_m - \frac{b\omega_m^2}{J_m}sgn(\omega_m) + \frac{T_m}{J_m} \tag{1}$$

$$\ddot{\theta_l} = -\frac{K_s}{J_l}\theta_l + \frac{K_s}{J_l}\theta_m + \frac{mgl}{J_l}\sin\theta_l \tag{2}$$

Using the state space variable representation, the state-space model for the plant dynamics can be defined.

$$\begin{bmatrix} x_1 \\ x_2 \\ x_3 \\ x_4 \end{bmatrix} = \begin{bmatrix} \theta_m \\ \theta_l \\ \dot{\theta_m} \\ \dot{\theta_l} \end{bmatrix}$$

$$\begin{bmatrix} \dot{x}_1 \\ \dot{x}_2 \\ \dot{x}_3 \\ \dot{x}_4 \end{bmatrix} = \begin{bmatrix} 0 & 0 & 1 & 0 \\ 0 & 0 & 0 & 1 \\ -\frac{K_s}{J_m} & \frac{K_s}{J_m} & 0 & 0 \\ \frac{K_s}{J_l} & -\frac{K_s}{J_l} & 0 & 0 \end{bmatrix} \begin{bmatrix} x_1 \\ x_2 \\ x_3 \\ x_4 \end{bmatrix} + \begin{bmatrix} 0 \\ 0 \\ -\frac{b\cdot\mathrm{sgn}(x_3)x_3^2}{J_m} \\ -\frac{mgl\sin(x_2)}{J_l} \end{bmatrix} + \begin{bmatrix} 0 \\ 0 \\ \frac{1}{J_m} \\ 0 \end{bmatrix} T_m \tag{3}$$

The relationship between the input voltage and torque can be identified using the electrical model for a permanent magnet DC motor as shown in figure 7.

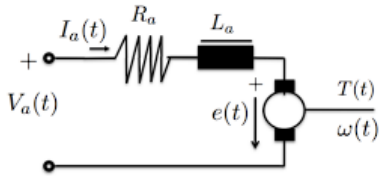

Figure 6: Electrical model for a permanent magnet DC motor

$$V_a = I_a R_a + L_a\frac{dI_a}{dt} + e$$
$$V_a = I_a R_a + L_a\frac{dI_a}{dt} + K_m\omega_m$$

$$\dot{I_a} = \frac{V_a}{L_a} - \frac{K_m\omega_m}{L_a} - \frac{I_a R_a}{L_a} \tag{4}$$

Now the state-space model for the plant and motor dynamics can be defined with the relationship $T_m = K_m I_a$.

$$\begin{bmatrix} x_1 \\ x_2 \\ x_3 \\ x_4 \\ x_5 \end{bmatrix} = \begin{bmatrix} \theta_m \\ \theta_l \\ \dot{\theta_m} \\ \dot{\theta_l} \\ I_a \end{bmatrix} \qquad u = V_a$$

$$\begin{bmatrix} \dot{x}_1 \\ \dot{x}_2 \\ \dot{x}_3 \\ \dot{x}_4 \\ \dot{x}_5 \end{bmatrix} = \begin{bmatrix} 0 & 0 & 1 & 0 & 0 \\ 0 & 0 & 0 & 1 & 0 \\ -\frac{K_s}{J_m} & \frac{K_s}{J_m} & 0 & 0 & \frac{K_m}{J_m} \\ \frac{K_s}{J_l} & -\frac{K_s}{J_l} & 0 & 0 & 0 \\ 0 & 0 & -\frac{K_m}{L_a} & 0 & -\frac{R_a}{L_a} \end{bmatrix} \begin{bmatrix} x_1 \\ x_2 \\ x_3 \\ x_4 \\ x_5 \end{bmatrix} + \begin{bmatrix} 0 \\ 0 \\ -\frac{\mathrm{b}\cdot\mathrm{sgn}(x_3)x_3^2}{J_m} \\ -\frac{mgl\sin(x_2)}{J_1} \\ 0 \end{bmatrix} + \begin{bmatrix} 0 \\ 0 \\ 0 \\ 0 \\ \frac{1}{L_a} \end{bmatrix} u \tag{5}$$

2.1 Motor Selection

To determine the maximum holding torque to inertia ratio required to hold the position of the arm at 60° stationary, the dynamics of the plant is considered. At stationary, we assume that $\theta_l = \theta_m$.

$$
\begin{aligned}
0 &= \frac{K_s}{J_m}\theta_l - \frac{K_s}{J_m}\theta_m + \frac{T_m}{J_m} \\
0 &= -\frac{K_s}{J_l}\theta_l + \frac{K_s}{J_l}\theta_m + \frac{mgl}{J_l}\sin\theta_l \\
T_m &= mgl\sin\theta_l \\
T_m &= (0.1kg)(9.81\frac{m}{s^2})(0.1m)\sin 60^\circ \\
T_m &= 0.08496Nm
\end{aligned}
$$

This means that motor 3 does not satisfy the requirements as its maximum starting torque is 0.0344Nm. Furthermore, motor 2 can produce 0.162Nm maximum torque, which is only double the minimum stationary torque. This means motor 2 will not be able to reliably carry out pick-and-place tasks. Motor 1 can produce 1.239Nm, the highest available torque output while maintaining a sufficient maximum angular velocity at $11.175\frac{rad}{s}$. We will analyse the voltage to torque mapping for motor 1 to ensure linearity.

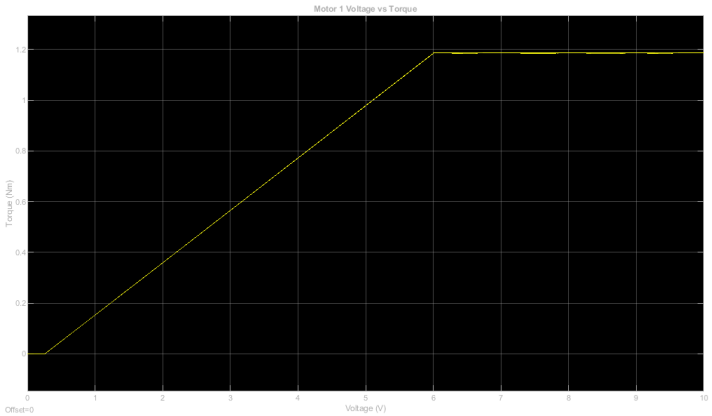

Figure 7: Voltage to torque relationship for motor 1

The output torque linearly rises to 1.2Nm from 0 to 6V. This linear performance means that motor 1 is the most suitable actuator for the plant.

3 Linear Model

Performing equilibrium analysis on the plant EOMs with equations 1 & 2:

$$
\begin{aligned}
0 &= \frac{K_s}{J_m}\theta_l - \frac{K_s}{J_m}\theta_m + \frac{T_m}{J_m} \\
0 &= -\frac{K_s}{J_l}\theta_l + \frac{K_s}{J_l}\theta_m + \frac{mgl}{J_l}\sin\theta_l \\
K_s\theta_l - K_s\theta_m + T_m &= -K_s\theta_l + K_s\theta_m + mgl\sin\theta_l
\end{aligned}
$$

Introducing Incremental variables $\tilde{x_1} = x_1 - x_{1e}$; $\tilde{x_2} = x_2 - x_{2e}$; $\tilde{x_3} = x_3$; $\tilde{x_4} = x_4$; $\tilde{x_5} = x_5 - x_{5e}$; $\tilde{u} = u - u_e$.

$$
\begin{bmatrix} \dot{\tilde{x_1}} \\ \dot{\tilde{x_2}} \\ \dot{\tilde{x_3}} \\ \dot{\tilde{x_4}} \\ \dot{\tilde{x_5}} \end{bmatrix} = \begin{bmatrix} \frac{\partial f_1}{\partial x_1} & \frac{\partial f_1}{\partial x_2} & \frac{\partial f_1}{\partial x_3} & \frac{\partial f_1}{\partial x_4} & \frac{\partial f_1}{\partial x_2} \\ \frac{\partial f_2}{\partial x_1} & \frac{\partial f_2}{\partial x_2} & \frac{\partial f_2}{\partial x_3} & \frac{\partial f_2}{\partial x_4} & \frac{\partial f_2}{\partial x_2} \\ \frac{\partial f_3}{\partial x_1} & \frac{\partial f_3}{\partial x_2} & \frac{\partial f_3}{\partial x_3} & \frac{\partial f_3}{\partial x_4} & \frac{\partial f_3}{\partial x_2} \\ \frac{\partial f_4}{\partial x_1} & \frac{\partial f_4}{\partial x_2} & \frac{\partial f_4}{\partial x_3} & \frac{\partial f_4}{\partial x_4} & \frac{\partial f_4}{\partial x_2} \\ \frac{\partial f_5}{\partial x_1} & \frac{\partial f_5}{\partial x_2} & \frac{\partial f_5}{\partial x_3} & \frac{\partial f_5}{\partial x_4} & \frac{\partial f_5}{\partial x_2} \end{bmatrix} \begin{bmatrix} \tilde{x_1} \\ \tilde{x_2} \\ \tilde{x_3} \\ \tilde{x_4} \\ \tilde{x_5} \end{bmatrix} + \begin{bmatrix} \frac{\partial f_1}{\partial u} \\ \frac{\partial f_2}{\partial u} \\ \frac{\partial f_3}{\partial u} \\ \frac{\partial f_4}{\partial u} \\ \frac{\partial f_5}{\partial u} \end{bmatrix} \tilde{u}
$$

$$\begin{bmatrix} \dot{\tilde{x}}_1 \\ \dot{\tilde{x}}_2 \\ \dot{\tilde{x}}_3 \\ \dot{\tilde{x}}_4 \\ \dot{\tilde{x}}_5 \end{bmatrix} = \begin{bmatrix} 0 & 0 & 1 & 0 & 0 \\ 0 & 0 & 0 & 1 & 0 \\ -\frac{K_s}{J_m} & \frac{K_s}{J_m} & -\frac{sgn(x_{3e})2x_{3e}b}{J_m} & 0 & \frac{K_m}{J_m} \\ \frac{K_s}{J_l} & -\frac{K_s}{J_l} - \frac{mgl\cos x_{2e}}{J_l} & 0 & 0 & 0 \\ 0 & 0 & -\frac{K_m}{L_a} & 0 & -\frac{R_a}{L_a} \end{bmatrix} \begin{bmatrix} \tilde{x_1} \\ \tilde{x_2} \\ \tilde{x_3} \\ \tilde{x_4} \\ \tilde{x_5} \end{bmatrix} + \begin{bmatrix} 0 \\ 0 \\ 0 \\ 0 \\ \frac{1}{L_a} \end{bmatrix} \tilde{u} \tag{6}$$

Since the system can be at equilibrium at any point with an appropriate motor torque T_m, the chosen linearisation point is at $x_{1e} = 45°$, $x_{2e} = 45°$. This point is chosen such that the incremental variables will have a maximum deviation of $\pm 15°$ since the controller steps up and down from 30° to 60° during operation. For the choice of Ks, the provided range of values provides a negligable difference to the performance of the linearised system, therefore, a value of 1.55 is chosen. Through the linearisation of the model, note that the damping term b is not considered in the linearised model since $x_{3e} = 0$ as it is a first-order term.

$$\begin{bmatrix} \dot{\tilde{x}}_1 \\ \dot{\tilde{x}}_2 \\ \dot{\tilde{x}}_3 \\ \dot{\tilde{x}}_4 \\ \dot{\tilde{x}}_5 \end{bmatrix} = \begin{bmatrix} 0 & 0 & 1 & 0 & 0 \\ 0 & 0 & 0 & 1 & 0 \\ -\frac{K_s}{J_m} & \frac{K_s}{J_m} & 0 & 0 & \frac{K_m}{J_m} \\ \frac{K_s}{J_l} & -\frac{K_s}{J_l} - \frac{mgl}{\sqrt{2}J_l} & 0 & 0 & 0 \\ 0 & 0 & -\frac{K_m}{L_a} & 0 & -\frac{R_a}{L_a} \end{bmatrix} \begin{bmatrix} \tilde{x_1} \\ \tilde{x_2} \\ \tilde{x_3} \\ \tilde{x_4} \\ \tilde{x_5} \end{bmatrix} + \begin{bmatrix} 0 \\ 0 \\ 0 \\ 0 \\ \frac{1}{L_a} \end{bmatrix} \tilde{u} \tag{7}$$

For the measurement matrix C, we use the camera sensor to measure the angle θ_l.

$$y = \begin{bmatrix} 0 & 1 & 0 & 0 & 0 \end{bmatrix} \begin{bmatrix} x_1 \\ x_2 \\ x_3 \\ x_4 \\ x_5 \end{bmatrix} \tag{8}$$

Using this state space representation, the transfer function of the linearised plant from the input voltage to the link angle can be identified with $\mathbf{G}(s) = \mathbf{C}(s\mathbf{I} - \mathbf{A})^{-1}\mathbf{B} + \mathbf{D}$

$$\mathbf{G}(s) = \frac{2.202\text{e}09}{\text{s}^5 + 1.444\text{e}04\ \text{s}^4 + 7.65\text{e}05\ \text{s}^3 + 3.405\text{e}07\ \text{s}^2 + 1.235\text{e}09\ \text{s} + 7.395\text{e}08} \tag{9}$$

Using partial fraction decomposition, we find the pole locations of the fifth order system at $p_1 = -14391$, $p_{2/3} = -4.45 \pm 43.83i$, $p_4 = -43.47$, $p_5 = -0.6089$

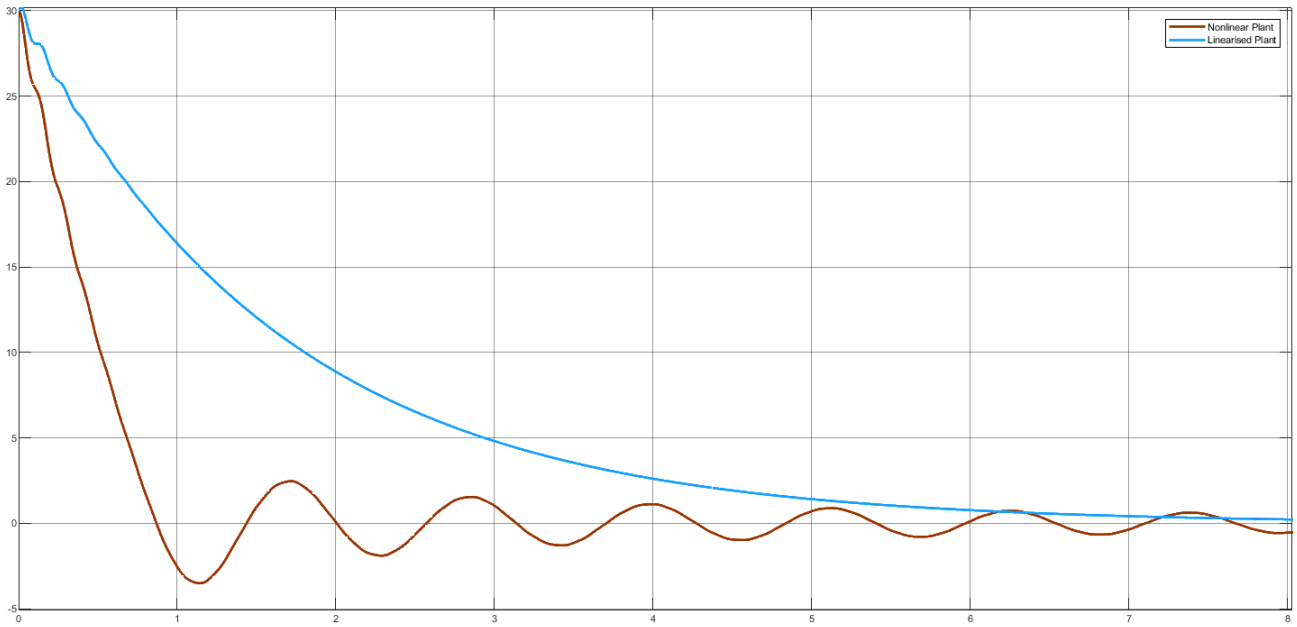

Figure 8: Comparison of the linearised and nonlinear plants

Using an inital angle of 30°, the free response of the linear and nonlinear plants have a large difference, with the linearised plant lacking oscillations during the settling process. This difference could be due to the lack of consideration for the damping term b and other simplifying assumptions about the nonlinear plant, such as a different motor torque constant than specified J_m.

4 Performance Requirements

The specifications for the physical non-linear system are the following parameters:

1. Maximum overshoot of at most 5 degrees.
2. Settling time of at most 2.0 seconds (for a less than 2% settling criterion).
3. Steady state error of at most 2 degrees.
4. Maximum controller sampling frequency of 50 Hz.

Looking at the complex domain pole locations of the fifth-order linear system, in figure 9, the system has 2 fast poles and can be approximated as a third-order system. Using pole placement design techniques in the complex domain for canonical second-order systems, we can provide an underlying design strategy for the provided specifications. Note that these design strategies are rough guidelines for design, especially since our system is a third-order system which behaves differently.

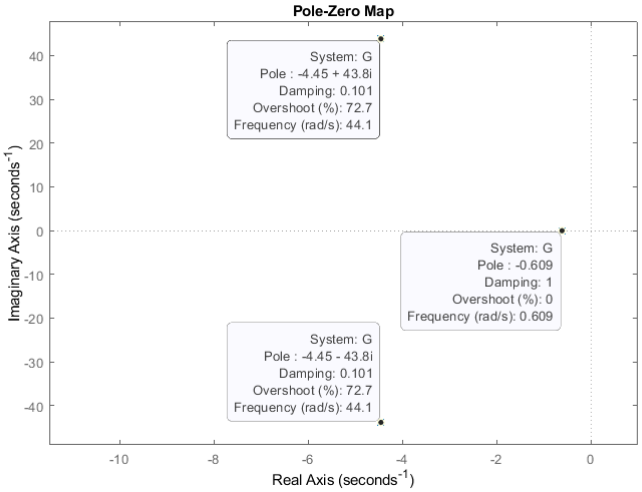

Figure 9: Dominant poles of the linearised system

For a maximum overshoot of at most 5 degrees, we can estimate a minimum overshoot percentage M_p when the system is at 60°. $M_p = \frac{5}{60} \times 100 = 8.33\%$. Using the relationship $M_p = \exp\left(\frac{-\pi\zeta}{\sqrt{1-\zeta^2}}\right)$, we obtain $\zeta = 0.62$. Therefore, the bound for the complex domain angle beginning at the imaginary axis is:

$$\arcsin 0.62 = 38.3^\circ \tag{10}$$

For a setting time of at most 2 seconds, the 2% settling time criterion is $\sigma \geq \frac{4}{t_s}$

$$\sigma \geq 2 \tag{11}$$

5 Controller Design

Using these design requirements on a Root Locus, we have the following pole restrictions on the linearised system.

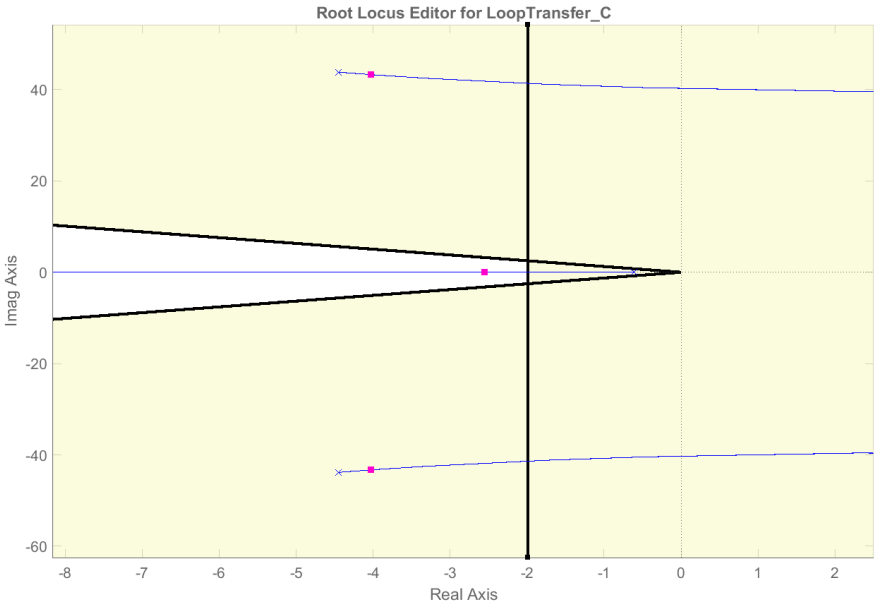

Figure 10: Root Locus of the linearised system

Initial inspection of the root locus shows that the two complex poles of the system move towards the unstable region with an increasing gain. This also demonstrates how the complex poles will not satisfy the overshoot requirements with purely an increasing gain.

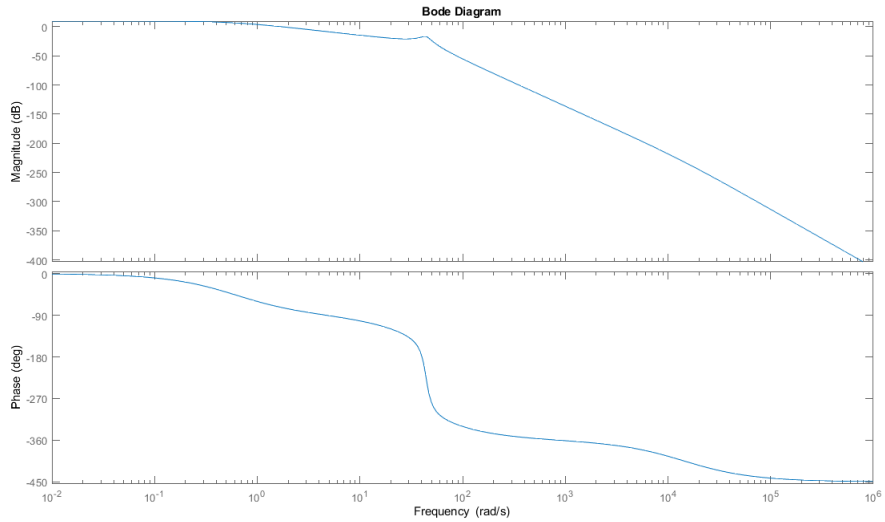

Figure 11: Bode Plot of the plant

Looking at the Bode plot of the plant, there is a small resonant peak at $45\frac{rad}{s}$. For the design of the gain, we need to ensure that the resonant peak is below 0dB such that there is no unstable behaviour and an appropriate gain margin. This gain must be before the resonant peak of the system because the phase margin drastically decreases after the peak. Using a proportional gain controller, the system does not achieve steady state convergence before unstable behaviour, therefore, we will add an integrator into the controller to achieve convergence. Furthermore, an additional zero is added to increase the phase margin before the resonant frequency. Using the maximum overshoot and settling time of the step response, a tuned PI controller is shown:

$$C(s) = 3.7 + \frac{1.667}{s}$$
$$C(s) = \frac{3.7(s + 0.6)}{s}$$

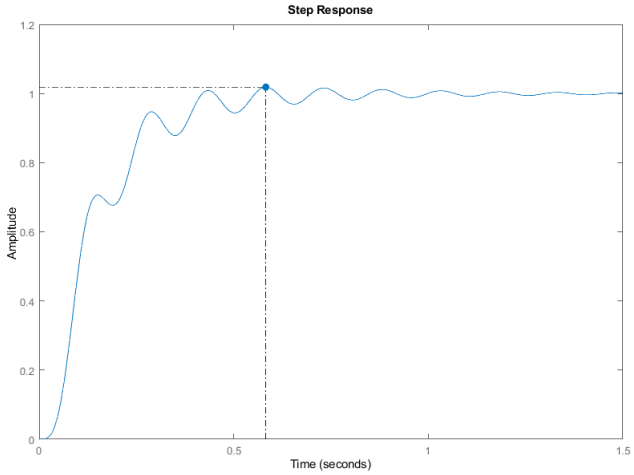

Figure 12: Step response for the tuned PI controller

Since the step response does not have a high overshoot, we do not need to include a derivative component in the controller. After tuning the parameters of the controller with a proportional gain component of 3.7 and an integral gain component of 1.667, the following parameters are found:

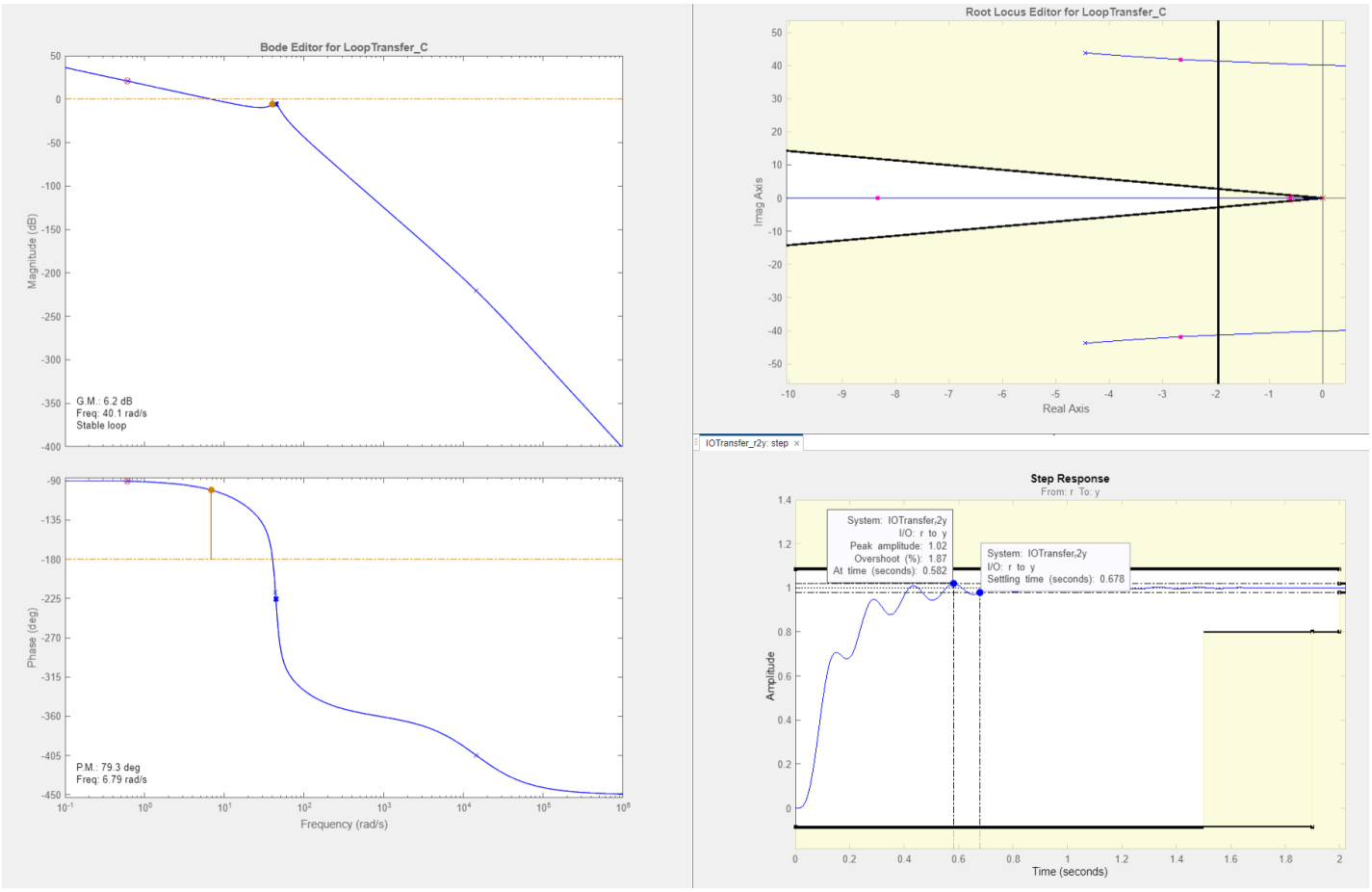

Figure 13: Bode Plot and Root Locus of the controller

From the designed PI controller, the system satisfies the maximum overshoot and settling time specifications with a 1.87% overshoot and 0.678 settling time, while maintaining a phase margin of 79.3° and a gain margin of 6.2dB with a crossover frequency of $6.8\frac{rad}{s}$. This phase and gain margin provide robustness to the controller, which is important since the controller will be used on the non-linear system. Although the pole placements do not adhere to the design specification guidelines for a second-order canonical system, the resulting step response meets the specifications because it is a higher-order system. Using this controller on the linear plant model, we obtain the following response:

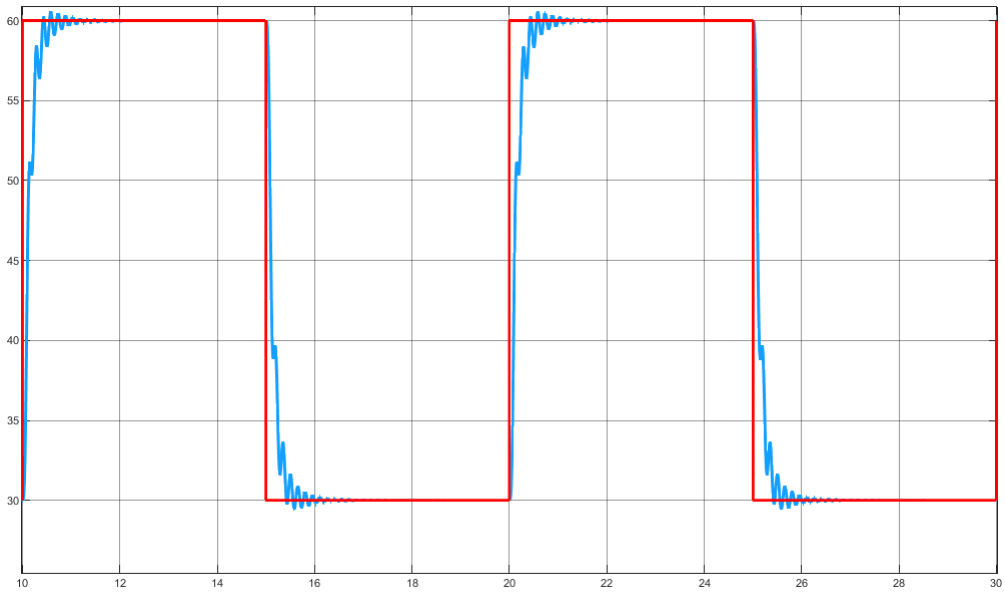

Figure 14: PI controller performance on the linearised plant

We can observe that the PI controller easily satisfies all the design parameters of overshoot, settling time and steady-state performance.

6 Digital Emulation

For the digital emulation of the controller, we perform three discretisation methods.

1. Zero-order hold
2. Euler method
3. Bilinear (Tustin) method

Using a sampling time of 0.02s corresponding to the controller frequency of 50Hz, the following performance on the linear plant is observed.

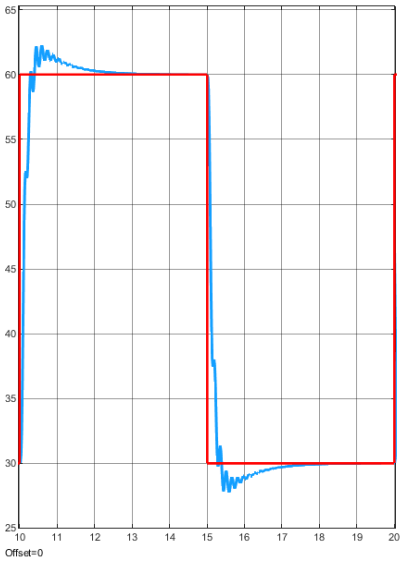

Figure 15: Zero-order hold

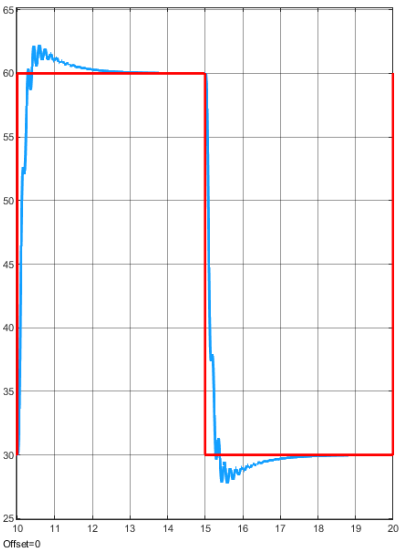

Figure 16: Euler Method

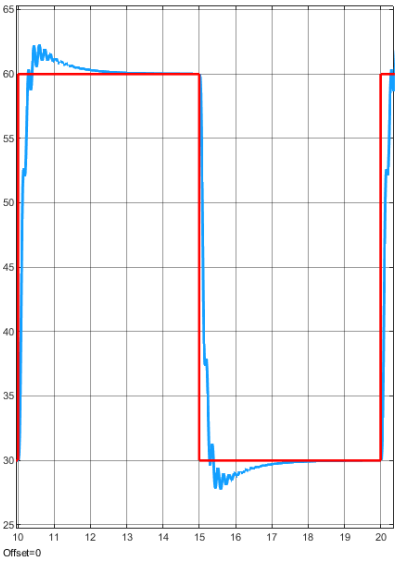

Figure 17: Bilinear transform

Using this sampling time, we can see that each discretisation method produces very similar outputs with negligible differences. As we increase the sampling time of the discrete controller, the oscillations of the system increase with a larger overshoot. At a certain sampling frequency, the system becomes unstable and does not acheive steady state convergence.

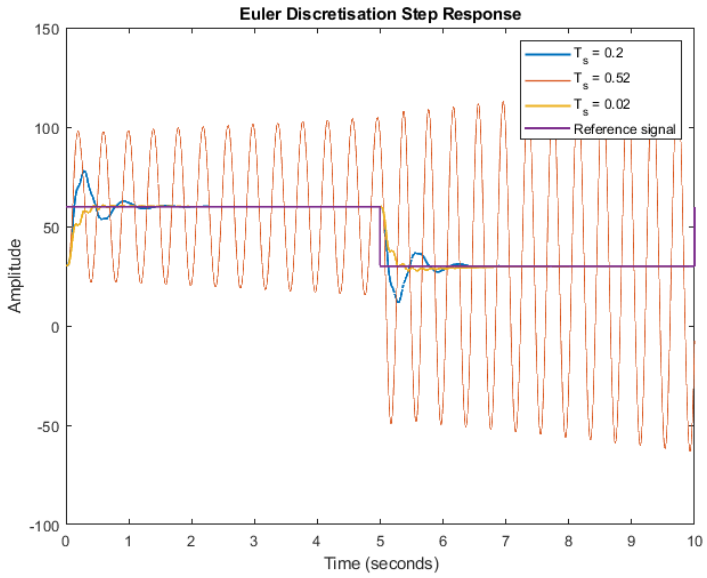

Figure 18: Euler Discretisation

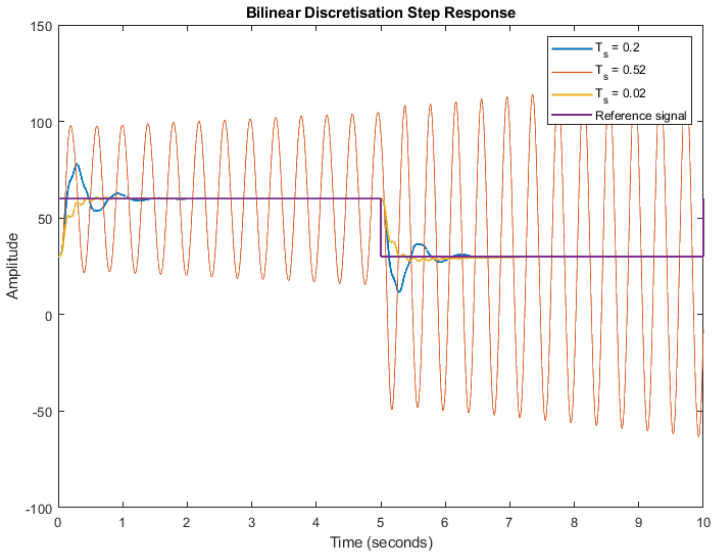

Figure 19: Bilinear Discretisation

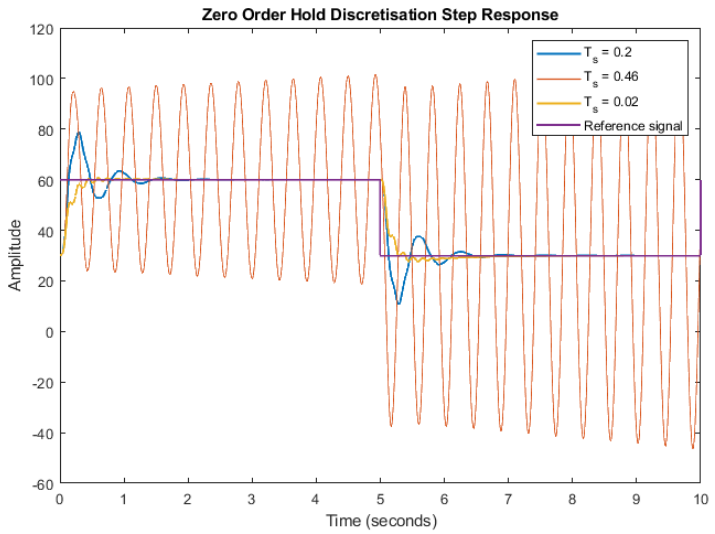

Figure 20: Zero Order Hold Discretisation

For the Euler and Bilinear discretisation methods, the sampling time that causes the system to become unstable is $T_s = 0.52$. For the Zero order hold discretisation, a sampling time of $T_s = 0.46$ causes the system to become unstable. This instability is due to aliasing, which is caused by a sampling time that is too low to capture the current state of the system, causing the system to become unstable due to the mismatch between the controller voltage input and the required voltage to reduce the error signal to 0.

7 Nonlinear Plant Performance

Using the Bilinear discretisation of the controller with $T_s = 0.02s$, we observe the response of the non-linear plant with the 50fps vision sensor in figure 21. The controller is able to meet the overshoot specifications of 5°, however, the measurement noise from the vision sensor means that this controller is unable to satisfy the 2% settling time and ±2° steady state error. Notably, there is a larger undershoot when moving from 60° to 30° compared to the overshoot moving from 30° to 60°. To account for this higher frequency measurement noise, a first order lowpass filter is implemented at a cutoff frequency of $25\frac{rad}{s}$. Using the bilinear transform discretisation of the lowpass filter $F(s) = \frac{25}{s+25}$, we obtain the following discrete LPF:

$$F(z) = \frac{0.2z + 0.2}{z - 0.6} \tag{12}$$

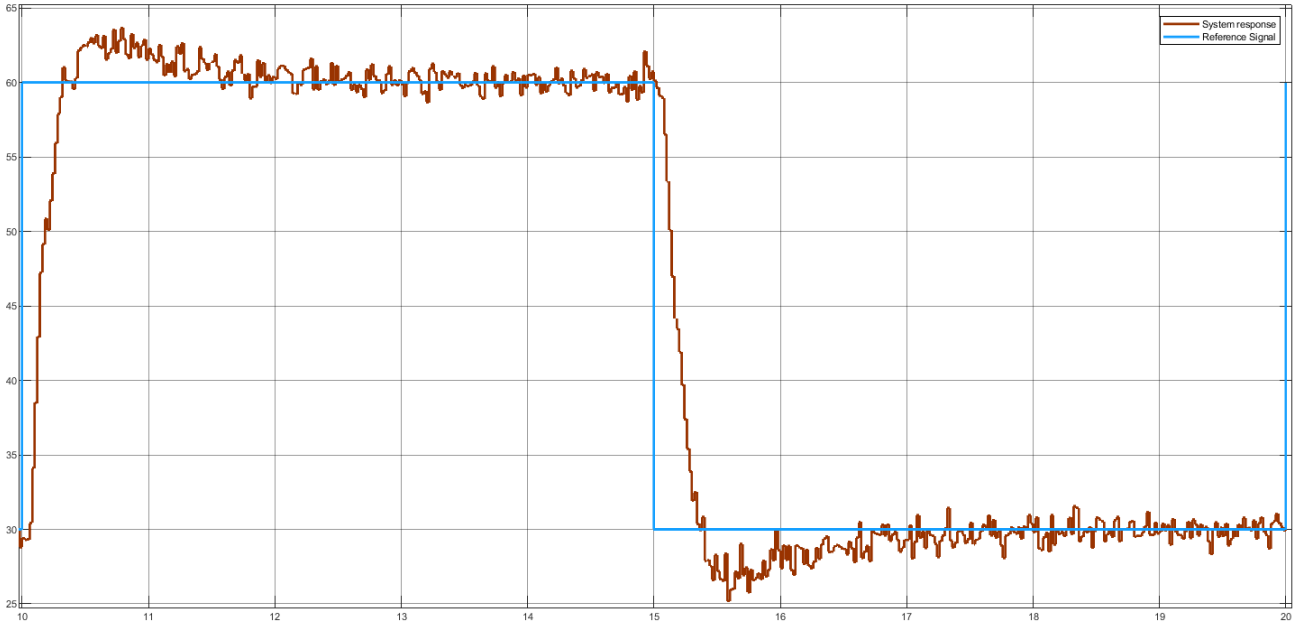

Figure 21: Nonlinear system response

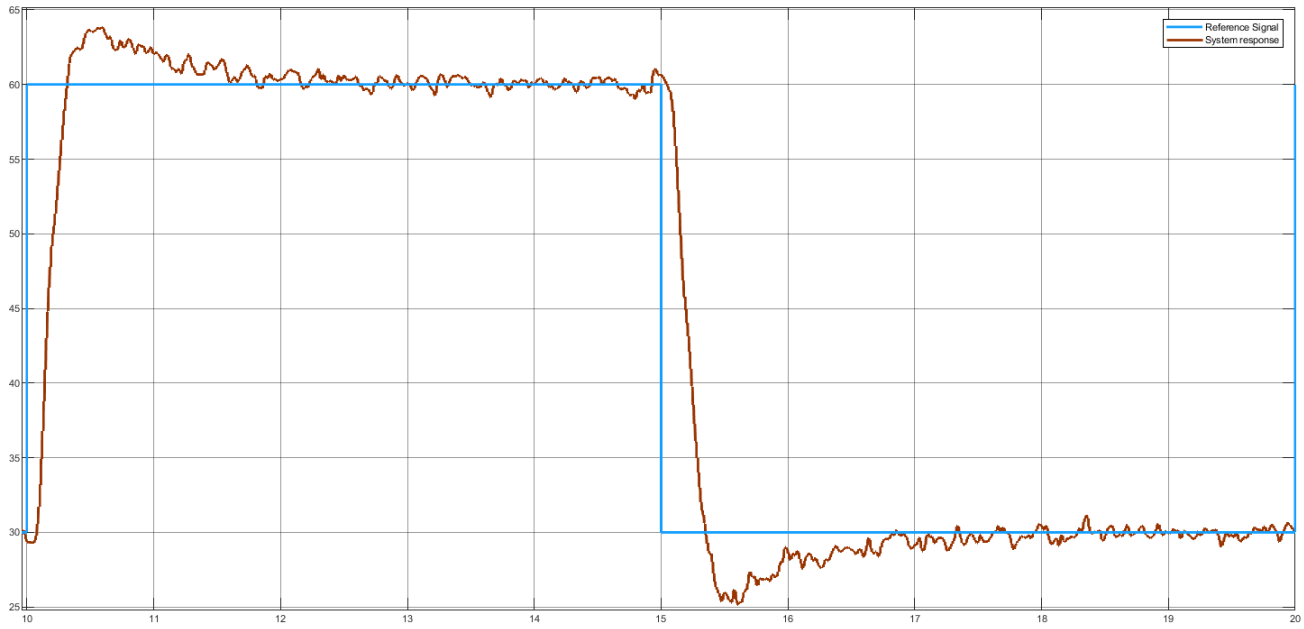

Figure 22: Nonlinear system response

8 Conclusion

Using the discretised lowpass filter in figure 22, the sharp jitters are reduced, allowing the controller to meet the $\pm 2°$ steady state error, however, the controller is not able to reach 2% settling time for a less than 2% settling criterion at the 30° reference due to the noise from the vision sensor. Comparing this response with the nonlinear plant in figure 14, the nonlinear system performs substantially worse, with much greater overshoot, settling time and a greater steady state error. Although the steady state error can be mainly attributed to the vision sensor measurement noise, the overshoot and settling time is a result of the linearisation being quite inaccurate as seen in figure 8, with no consideration of the friction term b that is removed during linearisation. Furthermore, the linearised model is performed at a link angle of 45°, this means that the increments around this linearised point of $\pm 15°$ could be too large to maintain a good linearisation of the nonlinear model. This problem could be addressed by having the nonlinear plant linearised at multiple points such as at 30°, 45° and 60°, using the appropriate model based on the vision sensor reading. Furthermore, we could reduce the variance from the vision sensor measurement noise by using sensor fusion with a gyro with a Kalman filter since the camera can be used to account for the drift in the gyroscope readings. This could be achieved using a 25fps camera and a gyro, which would provide better readings at a cheaper cost.